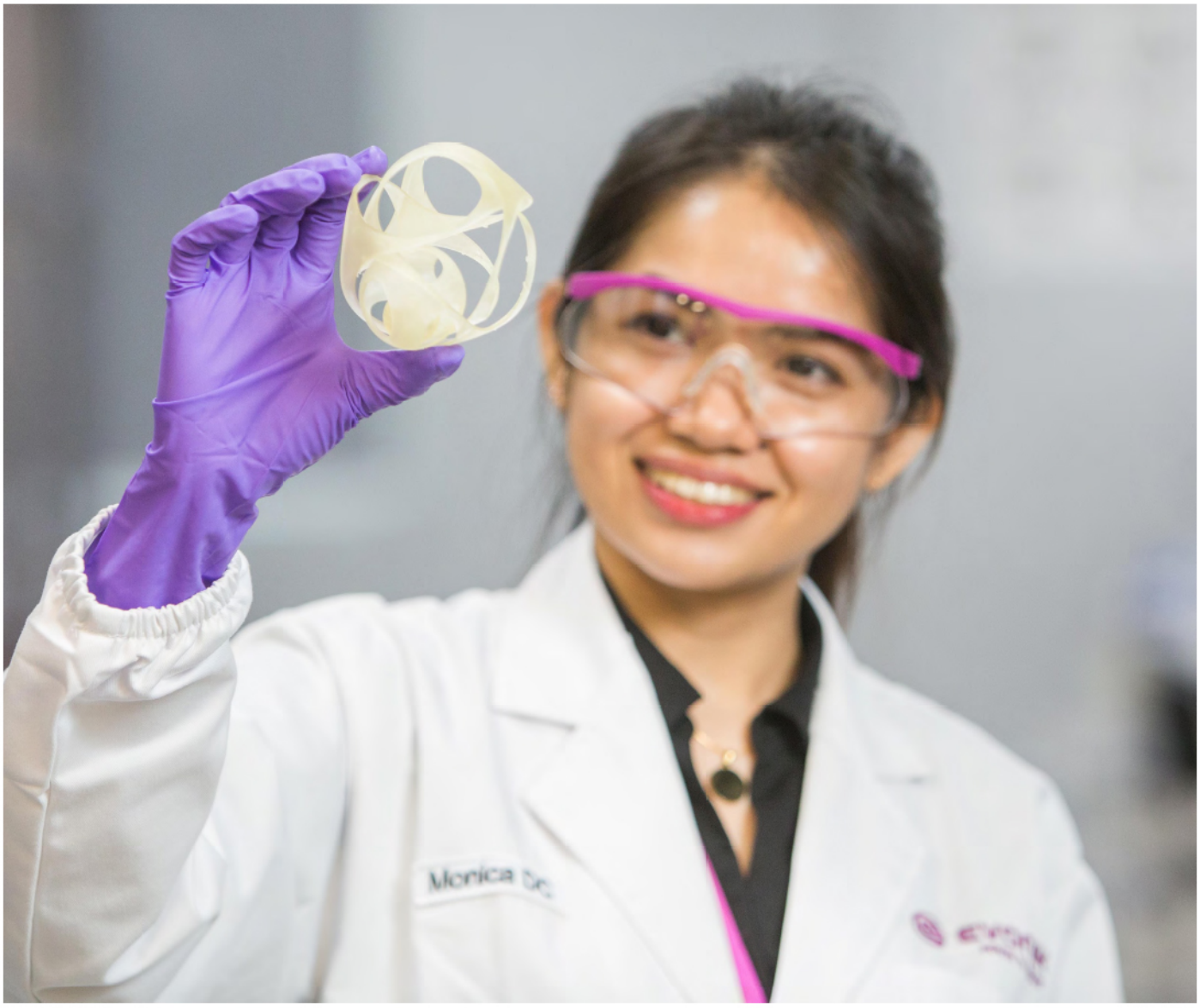

Pushing the boundaries of chemistry? It takes #HumanChemistry

Make your curiosity and talent as a chemist matter to the world with a specialty chemicals leader. Together, we combine cutting-edge science with engineering expertise to create solutions that answer real-world problems. Find out how our approach to technology creates more opportunities for growth, and see what chemistry can do for you at:

evonik.com/career

EVONIK
Leading Beyond Chemistry

ADVANCED HEALTHCARE MATERIALS
www.advhealthmat.de

$K_2Mn_3[Fe^{II}(CN)_6]_2$ NPs with High T_1-Relaxivity Attributable to Water Coordination on the Mn(II) Center for Gastrointestinal Tract MR Imaging

Murthi S. Kandanapitiye, Thiloka M. Dassanayake, Arosha C. Dassanayake, John Shelestak, Robert J. Clements, Can Fernando, and Songping D. Huang**

The lack of acid stability in the stomach and of temporal stability when moving through the gastrointestinal (GI) tract has made the development of oral magnetic resonance imaging (MRI) contrast agents based on the platform of Gd^{3+}–complexes problematic.On the other hand, the negative contrast enhancement produced by the T_2-weighted magnetic metal oxide nanoparticles (NPs) often renders the image readout difficult. Biocompatible NPs of the manganese Prussian blue analog $K_2Mn_3[Fe^{II}(CN)_6]_2$ exhibit extremely high stability under the acidic conditions of the gastric juice. Additionally, the high r_1 relaxivity, low toxicity, and high temporal stability of such NPs offer great potential for the development of a true T_1-weighted oral contrast agent for MRI of the entire GI tract.

1. Introduction

The tendency to form a blue colloidal sol in aqueous solution had long been noticed before the composition and structure of Prussian blue (PB) was identified.[1,2] Such properties, coupled with the nontoxic nature of PB, should position this remarkably stable polymeric coordination compound well for various medicinal and biomedical application.[3] The recent discovery that PB and its several analog compounds can act as T_1-weighted magnetic resonance imaging (MRI) contrast agents (CAs) at this and several other laboratories has sparked great research interests in their potential applications in the MRI, X-ray computed tomography (CT) and positron emission tomography (PET) imaging modalities, biomolecular sensing, metallodrug development, and cancer research.[4–15]

With the widespread applications of MRI in modern diagnostic medicine, the development of MRI contrast agents has emerged as an important research area in medicinal and bioinorganic chemistry.[16,17] An MRI CA is a paramagnetic compound that can preferentially shorten either the T_1 or the T_2 relaxation time of water protons in tissues.[18–20] From the clinical standpoint, T_1-weighted CAs are more suitable for diagnostic applications, as the image produced by a T_2-weighted CA is often difficult to interpret due to the interference of various artifacts from the background.[21] Currently, most T_1-weighted CAs in the clinical use are small-molecule Gd^{3+}–chelates.[17] All of them have relatively limited relaxivity values, i.e., several percents of the attainable values predicted by the Solomon–Bloembergen–Morgan (SBM) theory.[22,23] Furthermore, the significantly decreased thermodynamic stability of such Gd^{3+}–chelates in an acidic environment makes them unsuitable as oral CAs for imaging the gastrointestinal (GI) tract.[24] For example, a dimeglumine salt of Gd^{3+}–DTPA (diethylenetriaminepentaacetic acid; Magnevist Enteral) is only permitted for enteral or rectal rather than oral administration for imaging the bowel[24] due to the safety concern of gadolinium adsorption in the stomach.Since 1993 ammonium ferric citrate (AFC) has been introduced to clinical use as an oral T_1-weighted CA in Japan. The problem with AFC is that a large dose, i.e., 600–1200 mg in 600 mL of solution, needs to be used in order to obtain adequate contrast enhancement. Furthermore, the temporal stability of AFC is poor so that only the upper abdomen imaging in the GI tract can be obtained owing to a reduction of MR signals in the lower abdomen. As a result, this oral CA has never gained a widespread use outside Japan.[25] Interestingly, a specially formulated $MnCl_2$ aqueous solution (LumenHance) has been used as an oral T_1-weighted CA for imaging the GI tract. However, Mn^{2+} ions can readily be absorbed in the GI tract, which makes both the adequate distension of the small intestine and temporal stability of MR signals throughout the entire GI tract problematic.[26] Despite the intense research efforts made in the past two decades, there is still an unmet clinical need for reliable T_1-weighted oral MRI CAs for clinical applications in the GI tract imaging.[27]

M. S. Kandanapitiye, T. M. Dassanayake, A. C. Dassanayake, S. D. Huang
Department of Chemistry and Biochemistry
Kent State University
Kent, OH 44240, USA
E-mail: shuang1@kent.edu
M. S. Kandanapitiye, C. Fernando
Department of Nano Science and Technology
Wayamba University of Sri Lanka
Kuliyapitiya 60200, Sri Lanka
J. Shelestak, R. J. Clements
Department of Biological Sciences
Kent State University
Kent, OH 44240, USA
E-mail: rclement@kent.edu
The ORCID identification number(s) for the author(s) of this article can be found under https://doi.org/10.1002/adhm.202100987

DOI: 10.1002/adhm.202100987

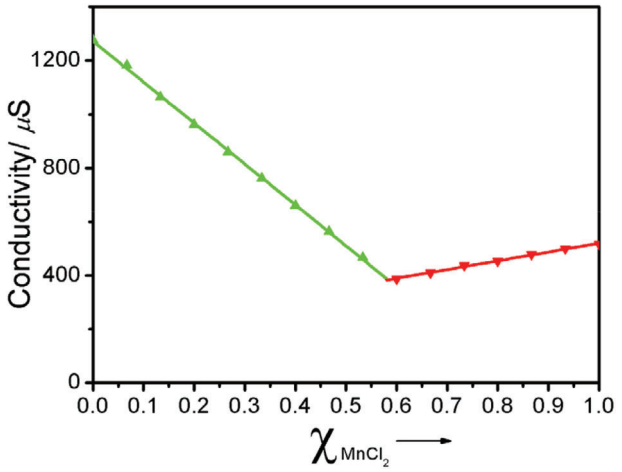

Figure 1. Job plot of the conductometric titration data for the combination of $MnCl_2$ with $K_4[Fe^{II}(CN)_6]$ in aqueous solution.

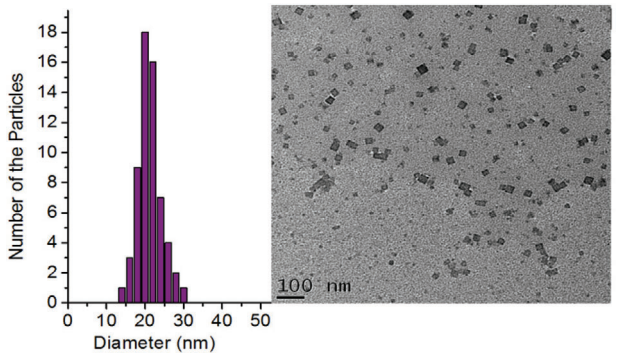

Figure 2. Histogram of the size distribution of MnPBA NPs (left) corresponding to the NPs measured from the TEM image (right).

In this article, we report on the synthesis, characterization, and MRI properties of $K_2Mn_3[Fe^{II}(CN)_6]_2$ nanoparticles (NPs). We demonstrate that due to a salient structural feature of this manganese analog of Prussian blue, the inner-sphere contribution to the T_1-relaxivity is activated, making such NPs a very effective T_1-weighed CA with an unusually high r_1 relaxivity value for a Mn(II) compound. Additionally, the 3D covalent network structure of $K_2Mn_3[Fe^{II}(CN)_6]_2$ ensures that the Mn^{2+}, Fe^{2+}, and CN^- ions are all tightly confined in their corresponding crystallographic positions. This feature is in sharp contrast with many high-spin Mn(II) complexes that possess modest thermodynamic stability and poor kinetic inertness, hence rendering $K_2Mn_3[Fe^{II}(CN)_6]_2$ an ideal structural platform for developing oral MR CAs with high temporal stability for imaging the entire CT tract.[28]

2. Results and Discussion

2.1. Synthesis and Characterization of NPs and the Bulk Sample of $K_2Mn_3[Fe^{II}(CN)_6]_2$

When $MnCl_2$ solutions with different concentrations were titrated with various volumes of $K_4[Fe^{II}(CN)_6]$ solutions, the equivalence point at the lowest electric conductivity revealed that the ratio of $MnCl_2$ to $K_4[Fe(CN)_6]$ is 3:2, as shown by the Job plot in **Figure 1**, suggesting the formula for the product of this manganese analog of PB to be $K_2Mn_3[Fe^{II}(CN)_6]_2$ (hereafter abbreviated as MnPBA). The preparation of citrate-coated MnPBA NPs was carried out with a simple aqueous solution reaction using trisodium citrate as the capping agent. Among several surface-coating or surface-capping agents including PEG (polyethylene glycol), PVP (polyvinylpyrrolidone), dextran, and methycarboxyl dextran tested, we found that the citrate anion gave the most satisfactory results in terms of the stability of MnPBA NPs against aggregation and the narrow size distribution.For characterization purposes, a bulk sample was also prepared with the same procedure but in the absence of trisodium citrate. The latter reaction yielded a pale-yellow solid after dialysis and lyophilization. The quantitative elemental analysis of MnPBA NPs and the bulk sample carried out by the inductive couple plasma spectroscopy (ICP) gave the relative molar ratios of K:Mn:Fe of 0.997:1.44:1.00 and 1.02:1.51:1.00, respectively, confirming the idealized formulas of these materials to be $K_2Mn_3[Fe^{II}(CN)_6]_2$ or $K_{0.67}Mn[Fe^{II}(CN)_6]_{0.67}$.

Transmission electron microscopy (TEM) imaging studies showed that the NPs were near cubic-shaped crystallites with an average size of 21 ± 3 nm, as determined by measuring and averaging the sizes of 61 NPs in the TEM frame shown in **Figure 2**.On the other hand, the presence of Mn, Fe, and K was confirmed by the energy dispersive X-ray spectroscopic (EDX) measurements performed on the several randomly selected individual NPs (Figure S1, Supporting Information).

X-ray powder diffraction (XRD) studies of the bulk sample resulted in the successful indexing of the compound to a monoclinic unit cell (space group $P2_1/c$) with the cell parameters a = 10.107(3) Å, b = 10.096(1) Å, c = 10.103(2) Å, β = 92.434°, and V = 1030.085 Å.[29,30] Since the single-crystal structure of this compound had not been reported, we used the atomic parameters of the monoclinic $KMn[Fe^{III}(CN)_6]$ as the structural model in the Rietveld refinement with site occupancies of the Wyckoff positions of the K^+ and $[Fe^{II}(CN)_6]^{4-}$ ions to be set at 2/3 to reflect the stoichiometry of the current compound (see Figure S2 and Tables S1 and S2 in the Supporting Information for results of the XRD structure refinement). In the crystal structure, the Mn(II) and Fe(II) centers are linked by the CN^- group to give rise to a Fe^{2+}–C≡N–Mn^{2+} coordinating motif. The carbon-bound Fe(II) center has low spin ($s_1 = 0$), but the nitrogen-bound Mn(II) center has high spin ($s_2 = 5/2$). Overall, each $K_2Mn_3[Fe^{II}(CN)_6]_2$ formula has a total of five unpaired electrons ($S_{total} = 5/2$). In order to satisfy octahedral coordination for both Mn(II) and Fe(II), the ratio of Mn^{2+}:Fe^{2+}:CN^- ought to be 1:1:6, as in the case of the prototypical model compound $KMn[Fe^{III}(CN)_6]$. However, in order to maintain electroneutrality in the Mn(II) analog of $[Fe^{II}(CN)_6]^{4-}$, 1/3 of the $[Fe^{II}(CN)_6]$ unit and 1/3 of the K^+ ion need to be absent from the crystal lattice to afford a neutral compound with the formula $K_2Mn_3[Fe^{II}(CN)_6]_2$. As a result, this unique stoichiometry not only creates large zeolitic cavities in the structure, but also produces an unusual coordination environment for the Mn(II) center, i.e., each Mn^{2+} ion is coordinated by four N atoms (2/3 × 6) from the CN^- groups of the nearby four $[Fe^{II}(CN)_6]$ units, and by two O atoms from two water molecules in a *cis*-configuration as shown in **Figure 3**. It should be noted that octahedral coordination of Fe(II) remains unchanged because the ratio of Fe^{2+}:CN^- is still 1:6. The water coordination to the Mn(II) center is the

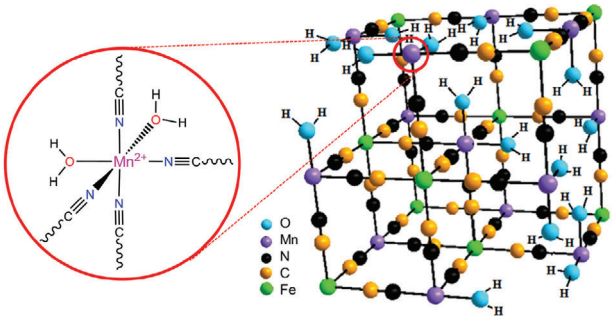

Figure 3. The structural model of $K_2Mn_3[Fe^{II}(CN)_6]_2$ based on the Rietveld refinement of the XRD patterns, illustrating the *cis*-water coordination to the Mn^{2+} ion.

origin of the active inner-sphere contribution to high T_1-relaxivity in this PB analog compound (vide infra).

Fourier transform infrared (FT-IR) spectra of both the bulk and NP samples showed the characteristic C≡N stretching vibration at 2060 cm^{-1} attributable to the Fe(II)–C≡N-Mn(II) bonding mode (Figure S3, Supporting Information).Additionally, the IR spectrum of MnPBA NPs exhibited the same spectroscopic features of free trisodium citrate, albeit with fewer peaks due to the restriction of certain vibration modes as often observed in metal citrate complexes. The large difference between the asymmetric and symmetric stretching vibrations of the carboxylate groups in MnPBA NPs, i.e., $\Delta[\nu_a(COO) - \nu_s(COO)] = 176$ cm^{-1} confirms that the citrate anion acts as a bidentate ligand to the metal center on the NP surfaces.[28] Thanks to the strong coordinating properties of citrate, MnPBA NPs surface-coated with this agent are highly dispersible in water as hydrated NPs with a hydrodynamic diameter of ≈100 nm based on the dynamic light scattering (DLS) measurements (Figure S4, Supporting Information).The thermogravimetric analysis (TGA) measurements showed that there were two types of water molecules present in the bulk sample. Specifically, the observed total weight loss of 14.11% from 77 to 162 °C corresponded to the loss of six water molecules from each $K_2Mn_3[Fe^{II}(CN)_6]_2{\cdot}6H_2O$ formula, which matches well with the calculated weight loss for six water molecules of 13.94%. This weight loss can be roughly divided into two steps, i.e., the first step from 77 to 135 °C is attributable to the loss of 2.5 zeolitic water molecules, while the second step from 135 to 162 °C is due to the loss of 3.5 coordinated water molecules (Figure S5, Supporting Information). The TGA curve of the citrate-coated MnPBA NPs showed an additional 21% weight loss compared to the TGA curve of the bulk sample, indicating that the average citrate coating on the NPs was ≈21% (Figure S6, Supporting Information). We found that the aqueous dispersion of such NPs could reach a concentration as high as 0.20 M of manganese and was stable at room temperature for as long as 6 months without aggregation.

2.2. Proton Relaxivity Measurements of Citrate-Coated MnPBA NPs

To assess the MR contrast effectiveness of MnPBA NPs, we measured the proton T_1 and T_2 relaxation times in order to obtain the relaxivity values, r_1 and r_2 at 1.4 T with the use of a Bruker MiniSpec relaxometer. The r_1 or r_2 relaxivity is the increase of T_1 or T_2

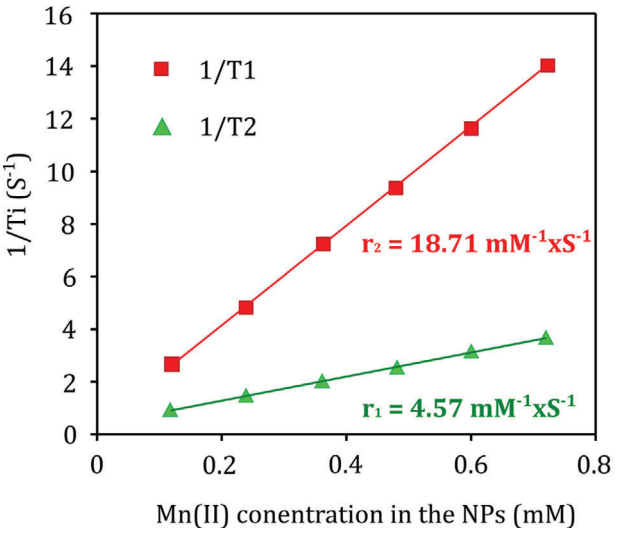

Figure 4. Plots of $1/T_i$ (i = 1, 2) versus Mn (II) concentration at 1.4 T for citrate-coated MnPBA NPs.

relaxation rate of the bulk water protons per 1×10^{-3} M of the CA used. Since the Mn^{2+} ion is the only paramagnetic center in the NPs, the change in both T_1 and T_2 relaxation rates with increasing concentration of Mn^{2+} ions in $\times 10^{-3}$ M was experimentally measured to yield the r_1 and r_2 relaxivity values by plotting $1/T_1$ or $1/T_2$ versus the concentration of Mn^{2+} ions using the following equation

$$\frac{1}{T_{i,\text{obs}}} = r_i \times [\text{Mn}] + \frac{1}{T_{i,\text{d}}} \quad (i = 1, 2) \tag{1}$$

where $1/T_{i,d}$ (i = 1, 2) is the diamagnetic contribution to the relaxation rate, and [Mn] is the concentration of Mn^{2+} ions in NPs. As shown in **Figure 4**, the measured values for these NPs were $r_1 = 4.57$ mM^{-1} s^{-1} and $r_2 = 18.71$ mM^{-1} s^{-1} at 1.4 T, resulting in an r_2/r_1 ratio of 4.09. This ratio is typically used as an indicator to determine whether an MR CA is suitable for T_1-weighted contrast enhancement. With the theoretical limit of the r_2/r_1 ratio being unity, the smaller the ratio, the better an agent can act as a T_1-weighted CA. For example, the typical r_2/r_1 ratio is larger than 10 for most metal-oxide-based NPs due to their superparamagnetic nature, which makes metal-oxide-based NPs unsuited for T_1-weighted contrast enhancement.[31,32] Overall, the measured results place our citrate-coated MnPBA NPs on the top of all known Mn(II)-containing MRI CAs in terms of the large r_1 relaxivity value coupled with a favorable r_2/r_1 ratio. Consistent with our findings, G. Paul and co-workers recently reported on a series of solid-solution NPs of indium Prussian blue analog doped with Mn^{2+} ions, $K_{4y-3+x}Mn^{II}{}_xIn^{III}{}_{1-x}[Fe^{II}(CN)_6]_y$ NPs ($0.05 < x < 0.9$), and found that the r_1 relaxivity values in such NPs can range from 9 to 15 mM^{-1} s^{-1} per Mn^{2+} basis at 1.5 T from $x = 0.3$ to $x = 0.05$, respectively.[11]Furthermore, Cheng and coworkers found that Mn^{2+}-doped PB nanocubes exhibit increased r_1 relaxivity values ranging from 5.7 to 7.6 mM^{-1} s^{-1} depending on the level of Mn^{2+} doping.[33] It should be noted that the relaxivity values of Gd–DTPA are $r_1 = 3.4$ mM^{-1} s^{-1} and $r_2 = 3.7$ mM^{-1} s^{-1} at 1.5 T. On the other hand, the relaxivity values of the

Table 1. Comparison of relaxivity data of several selected MRI contrast agents.

MRI contrast Agent	Magnetic field [T]	r_1 [mM^{-1} s^{-1}]	r_2 [mM^{-1} s^{-1}]	r_2/r_1	Ref.
$K_2Mn_3[Fe^{II}(CN)_6]_2$ NPs	1.4	4.57	18.71	4.09	This work
$K_{4y-3+x}Mn^{II}_xIn^{III}_{1-x}[Fe^{II}(CN)_6]_y$ NPs	1.5	9	15	6.56	[11]
Mn^{2+}-doped PB NPs	1.5	5.7	7.6		[33]
Hollow MnO NPs	3	1.42	7.74	5.45	[21]
Gd–(DTPA) complex	1.4	3.4	3.7	1.1	[17]

commercial CA based on manganese(II) dipyridoxaldiphosphate (Teslascan) are $r_1 = 2.8$ mM^{-1} s^{-1} and $r_2 = 3.9$ mM^{-1} s^{-1} at 1.5 T (see **Table 1**).

We attribute the large r_1 value in the citrate-coated MnPBA NPs in large part to the water coordination on the Mn(II) center, which makes the inner-sphere contribution to T_1-weighted relaxivity active. In the SBM theory,[22] inner-sphere relaxation in molecular Gd^{3+}–chelates is understood from the following equation

$$R_{1p}^{is} = \frac{q[C]}{55.6\left(T_{1M} + \tau_M\right)} \quad (2)$$

where q is the number of water molecules coordinated to the Gd^{3+} center, [C] is the concentration of the CA in $\times 10^{-3}$ M, T_{1M} is the longitudinal relaxation time of the bound water, and τ_M is the mean residence lifetime of the coordinated water molecules. If T_{1M} and τ_M are kept constant, when the number of water molecules bound to the Gd^{3+} center is increased from one to two can double the inner-sphere T_1-weighted relaxivity. It should be noted that all the commercial Gd^{3+}–chelates contain only a single coordinated water molecule. It is not unreasonable to assume that the coordination of two water molecules to the Mn(II) center in these citrate-coated MnPBA NPs plays a crucial role in the increase of the inner-sphere T_1-weighted relaxation of the water protons.

2.3. Stability of MnPBA NPs in Aqueous Solution

We studied the thermodynamic stability of the bulk $K_2Mn_3[Fe^{II}(CN)_6]_2$ sample by determining its solubility product constant with a static method. A bulk sample was added to deionized water and stirred slowly at 25 °C for 48 h to reach equilibrium. The concentrations of both Mn^{2+} and Fe^{2+} ions in the solution were analyzed by atomic absorption spectroscopy (AAS; see the "Experimental Section" for details). The solubility product constant obtained from such measurements was found to be $(3.5 \pm 1.4) \times 10^{-38}$ mol^7 L^{-21}. The high thermodynamic stability of this coordination polymer is attributed to the robust 3D network structure where Mn^{2+}, Fe^{2+}, and CN^- ions are all locked in their lattice positions due to the large lattice energy. Despite the high thermodynamic stability, surface metal ions and ligand molecules could still be susceptible to substitution reactions if the compound lacked sufficient kinetic inertness. Therefore, the release of Mn^{2+} and CN^- ions from citrate-coated MnPBA NPs under the physiologically relevant conditions was also measured. To simulate the real in vivo conditions, the surface Mn^{2+} and CN^- ions were challenged by the presence of other essential metal ions and biological ligands including Ca^{2+}, Mg^{2+}, Zn^{2+}, phosphate from the phosphate-buffered saline (PBS) system r, bicarbonate, and 0.1 M HCl (pH = 1.0, i.e., similar to the acidity of gastric juice).The highest concentration of Mn^{2+} ions leached from the NP surfaces was 4.0 ± 1 ppm, while the lowest concentration was below 0.5 ppm (Figure S7, Supporting Information). These concentrations are much lower than the allowable concentration of Mn^{2+} ions in drinking water recommended by the US Environmental Protection Agency (EPA) at 0.050 mg L^{-1} or 50 ppm.[34] In other words, the use of these NPs as an oral MR CA would expose the patient to a lower level of manganese than the daily consumption of drinking water does. We also found that the highest concentration of CN^- leached to solution after 24 h soaking under these conditions was 0.25 ± 5 ppm (Figure S8, Supporting Information). This level of cyanide exposure by the patient is similar to the allowable concentration of cyanide in the drinking water, which is determined by the US EPA to be not harmful to humans or animals, as the mitochondrial enzyme, Rhodanese, can rapidly convert cyanide into thiocyanate.[35,36] In nature, a number of plants and fruit seeds can release free cyanide ions into water.

2.4. Cytotoxicity and Cellular Uptake of MnPBA NPs

Cytotoxicity of MnPBA NPs was assayed in HeLa cells by the 3-[4,5-dimethylthialzol-2-yl]-2,5-diphenyltetrazolium bromide (MTT) method. First cells were incubated for 24 h at 37 °C under 5% CO_2 with varying concentrations of NPs suspended in PBS. All cell viability assays were conducted in triplicate with the results given in **Figure 5**. We found that >80% of the cells were viable after 24 h of incubation with the citrate-coated MnPBA NPs at the concentration of 0.8×10^{-3} M, indicating that these NPs were nontoxic to mammalian cells. This concentration greatly exceeded the required concentration for producing sufficient contrast in the in vivo studies (i.e., $\approx 0.20 \times 10^{-3}$ M). The non-cytotoxic nature of such NPs could be attributable to their high structural integrity and proper surface protection.

Since cellular internalization of citrate-coated MnPBA NPs was considered a prerequisite for their potential use as a cellular probe for early cancer detection in the GI system, the cellular uptake of the NPs in HeLa cells was visualized using the fluorescence dye-labeled NPs in combination with the fluorescent confocal scanning microscopy. To image live cells after the internalization of the NPs, HeLa cells were first incubated with the 6-carboxyfluorescein (CbF) dye-labeled NPs for 3 h at 37 °C (see the "Experimental Section" for details of the dye-labeling procedure).

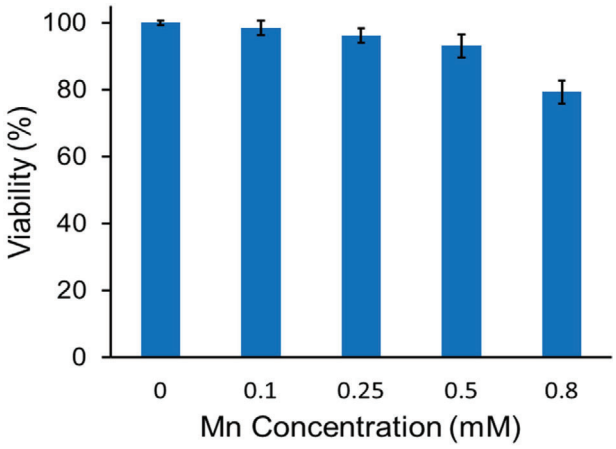

Figure 5. Viability curve of HeLa cells treated with citrate-coated MnPBA NPs with different concentrations (data presented as mean ± s.d., $n = 3$ replicates). $^*p < 0.01$ versus control.

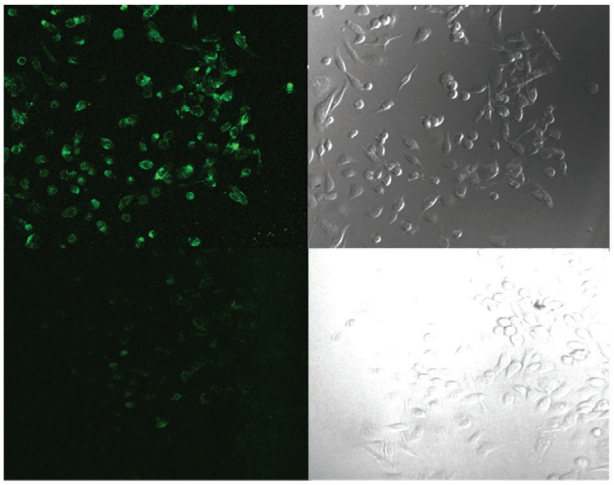

Figure 6. Fluorescence and bright-field images of the HeLa cells treated with dye-conjugated NPs for 3 h (upper left and right frames); fluorescence and bright-field images of the untreated cells as the control (lower left and right frames).

The cells were then washed with the PBS buffer three times to remove the uninternalized NPs prior to the direct imaging of live cells without fixation with the 488 nm excitation wavelength. As shown in **Figure 6**, the strong green fluorescent signals were clearly seen in the cytoplasm of the NP-treated HeLa cells, indicating that the CbF dye-conjugated MnPBA NPs were readily internalized by HeLa cells, while the much weaker fluorescent signals were detected in the untreated HeLa cells that were used as the negative control.

2.5. In Vivo MRI Studies of the GI Tract Using MnPBA NPs

To evaluate the ability of the MnPBA NPs to provide meaningful gut contrast in vivo, sequential MRI data were acquired before and every 15 min after during ingestion of the contrast agent. The NPs were mixed with corn oil and fed to the mouse after the first imaging timepoint with a gavage needle. MR image stacks

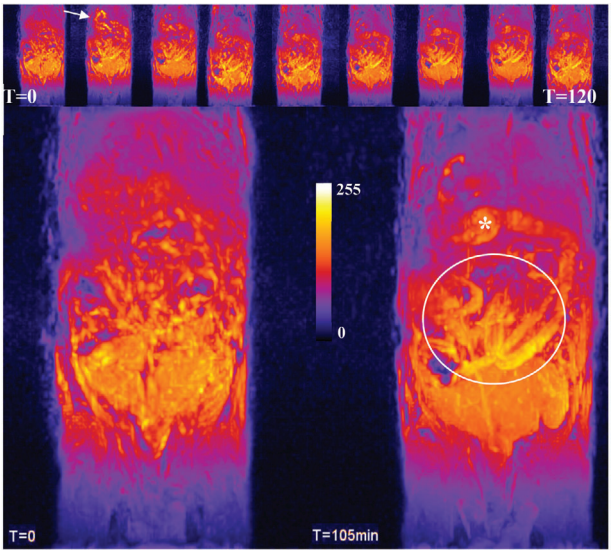

Figure 7. Sequential MRI data. About 11 image slices were *z*-compressed using a maximum intensity projection and a color lookup table applied to represent the data (color bar, middle). The top row depicts data acquired every15 min following gavage immediately after $T = 0$ until $T = 120$ min. Immediately after gavage, the contrast agent can be seen in the stomach as hyperintense (white arrow, second image top row). As the experiment progressed the hyperintense region moved through the GI tract and by 105 min the structure of the GI tract was clearly visible including the cecum (asterisk, lower right) and small intestines (circle, lower right).

were acquired spanning the body of the mouse to ensure the region of interest was captured (stomach, small intestine, and large intestine). Coincident image slices were compared across timepoints to evaluate movement of the contrast agent through the GI tract and any attained contrast. The images corresponding to the region of interest were extracted and *z*-compressed using a maximum intensity projection and a color lookup table applied to the data for each acquisition. Immediately after the gavage, at the 15 min imaging timepoint, the contrast agent can clearly be visualized as hyperintense within the stomach region as compared to timepoint 0. As the experiment progressed, the applied contrast agent moved through the GI tract, and, by the 105 min timepoint, additional structures, including the small intestines and cecum, were clearly visible (see **Figure 7**). These results show that MnPBA NPs as an MR CA possess not only high r_1 relaxivity but also high temporal stability for imaging the entire CT tract.

After the experiment was completed, the animal was allowed to recover and placed back into housing in the animal facility. The mouse displayed no adverse side effects from the MnPBA NPs' dose before, during, or after the experiments. The ability to provide contrast enhancement for resolving the GI anatomy using our imaging system with relatively low field strength (1 T) suggests that these methods should scale well with higher field strength magnets.

3. Conclusion

Although the investigations into using Mn(II) compounds as MRI CAs predate the advent of the commercial Gd3+–chelates, the modest thermodynamic stability and poor kinetic inertness

of the most high-spin Mn(II) complexes have thus far limited the success of such applications. In this work, we have successfully demonstrated that $K_2Mn_3[Fe^{II}(CN)_6]_2$ represents a unique structural platform for developing the Mn(II)-based NPs as an effective oral MRI CA with a large r_1 relaxivity value and extremely high stability under acidic conditions. We have also shown that the citrate-coated NPs can readily penetrate the cell membrane, thus opening the possibility of using them as a cellular MR probe for early cancer detection in the GI tract. Further research on the development of such NPs to fill the gap in the clinical GI tract imaging by the MRI modality is undoubtedly warranted.

4. Experimental Section

Materials: All chemicals were purchased from Sigma–Aldrich and used as received without further purification. HeLa cells were obtained from the American Type Culture Collection (Rockville, MD, USA) and kept at −200 °C prior to cell culture studies. Cell culture and all other cellular experiments were performed at 37 °C under an atmosphere of 5% CO_2 using the Dulbecco's modified eagle medium (DMEM) that was supplemented with 100 U mL^{-1} penicillin, 100 μg mL streptomycin^{-1}, 10% fetal bovine serum, 2.2 g L^{-1} $NaHCO_3$, 1×10^{-3} M sodium pyruvate, and 0.25 μg mL^{-1} amphotericin.

All the in vivo imaging studies using live animals were carried out in full compliance with the institutional guidelines as approved by the institutional IACUC committee.

Synthesis of Citrate-Coated MnPBA NPs and the Bulk MnPBA Sample: An aqueous solution of $MnCl_2$ (1×10^{-3} M, 15 mL) containing 100 mg of trisodium citrate was added dropwise to another aqueous solution of $K_4[Fe(CN)_6]$ (1×10^{-3} M, 10 mL) under vigorous stirring for ≈2 h. The product was then dialyzed in a tubular membrane bag made of regenerated cellulose (MWCO = 12 000–14 000) for 24 h, followed by lyophilization to obtain a solid product. The bulk $K_2Mn_3[Fe^{II}(CN)_6]_2$ sample was also prepared via the same procedure without the use of trisodium citrate as the capping agent. Specifically, an aqueous solution of $MnCl_2$ (1×10^{-3} M, 75 mL) was rapidly mixed with another aqueous solution $K_4[Fe(CN)_6]$ (1×10^{-3} M, 50 mL) at room temperature under vigorous stirring. The resultant pale-yellow solution turned cloudy after continuous stirring for ≈60 min. After dialysis, the solution containing the precipitate was dialyzed to afford an off-white powder.

TEM Imaging and EDX Elemental Analysis: The TEM imaging and EDX elemental analysis were conducted using an FEI Tecnai F20 TEM instrument equipped with a field emission gun operating at 200 kV. First, the lyophilized solid sample was suspended in water. Second, two droplets were transferred onto a carbon-coated copper TEM grid (400 mesh) and left at room temperature to dry on the grid in air in a covered container. The EDX elemental analysis results were obtained using an integrated scanning TEM (STEM) unit attached with an EDAX spectrometer.

Conjugation of Fluorescence Dye Molecules onto the Surfaces of Citrate-Coated MnPBA NPs: The fluorescence dye, 6-carboxyfluorescene, was conjugated to the surfaces of NPs using the *N*-[3-(dimethylamino)propyl]-*N*-ethylcarbodiimide hydrochloride (EDC)-coupling reaction. First, trisodium citrate (100 mg) and ethylenediamine (1×10^{-3} M, 1.0 mL) were added to an aqueous $MnCl_2$ solution (1×10^{-3} M, 15 mL). To this solution, an aqueous solution of $K_4[Fe(CN)_6]$ (1×10^{-3} M, 10 mL) was added and stirred for ≈3 h, followed by dialysis and lyophilization. Separately, 6-carboxyfluorescene (CbF, 0.012 g) was allowed to react with EDC (0.004 g) in a water/ethanol mixture (3.2×10^{-3} M, 10 mL) for 2 h. Finally, the primary NH_2 group on the surfaces of $K_2Mn_3[Fe^{II}(CN)_6]_2$ (10 mL, ≈3×10^{-3} M) NPs was conjugated with CbF using about 1 mL of the EDC-coupled CbF dye molecules under stirring for 12 h. The resulting mixture was then dialyzed for 2 days to remove unbound dye molecules. The fluorescence spectrum of the dye-conjugated NPs was collected to confirm the NP surface conjugation of the dye molecules.

The Cell Viability Assay: Cytotoxicity of citrate-coated MnPBA NPs was evaluated in HeLa cells using an MTT assay. First, cells were seeded at a density of 2×10^4 cells per well using a 96-well plate. Second, the cells were incubated for 5 h at 37 °C using the DMEM low glucose medium in an atmosphere of 5% CO_2 and 95% air. Third, the cells were then treated with a fresh medium (100 µL) mixed with varying amounts of NPs, followed by incubation for 24 h. Fourth, a medium containing 0.1 mg mL^{-1} of the MTT dye was added to each well and incubated for 3 h. Finally, after the MTT solution was removed, the precipitated violet dye crystals were dissolved in dimethyl sulfoxide (DMSO; 200 µL). Each assay was run in triplicated and the results were averaged.

Internalization of Citrate-Coated MnPBA NPs in HeLa Cells: The internalization of citrate-coated MnPBA NPs in HeLa cells was visualized under a confocal fluorescence microscope that monitored the cellular uptake of the dye-labeled MnPBA NPs. First, cells were seeded in at a density of ≈2×10^4 cells per well on an 8-well chamber slide, followed by 24 h incubation. Second, a medium containing dye-labeled NPs at the concentration of ≈100×10^{-6} M was added to each well to replace the initial culture medium. Third, the cells were incubated for 3 h and then washed with PBS three times to remove the uninternalized NPs. Finally, fresh medium was added to each well, and the live cells were imaged without fixation.

Determination of the Solubility Product (K_{sp}) Value of the Bulk MnPBA Sample and the Stability of Citrate-Coated MnPBA NPs Against the Leaching of Mn^{2+} and CN^- Ions: A bulk sample (≈800 mg) was first allowed to equilibrate with 1000 mL of deionized water at 25 °C for 48 h. The leachate was evaporated to dryness, calcined at 630 °C for 6 h, and then treated with nitric acid before the concentrations of metal ions were analyzed by AAS. The solubility product constant of $K_2Mn_3[Fe^{(II)}(CN)_6]_2$ was found to be $(3.5 \pm 1.4) \times 10^{-38}$ mol^7 L^{-21}. In other words, the equilibrium manganese ions' concentration was found to be $[Mn^{2+}] = (4.5 \pm 1) \times 10^{-6}$ M. For Mn^{2+} and CN^- ion leaching studies, the NP samples dispersed in deionized water (≈5 mL of 3×10^{-3} M) were each placed in a dialysis bag (MWCO = 3500) and soaked in a 50 mL solution containing one of the following species: 100 ppm Mg(II), 100 ppm Ca(II), 100 ppm Zn(II), 100 ppm HCO_3^- ions, or an acidic solution with pH ≈ 1. The dialysis bags were tightly sealed and incubated at 37 °C for 48 h. The leachates were analyzed for manganese by atomic absorption spectroscopy. Similarly, a set of separate NP samples dispersed in deionized water was used to study the leaching of CN^- ions under the physiological conditions. The resulting solutions were analyzed for free CN^- ions by a fluorometric method using the cyanide test kit developed by LaMotte Co. (Chestertown, MD; Code 7387-01). The calibration curve was established using the standard KCN solutions with the concentrations at the ppm level.

T_1 and T_2 Measurements: The longitudinal (T_1) and transverse (T_2) relaxation times of water protons induced by citrate-coated MnPBA NPs were measured using a Bruker minispec mq60 contrast agent analyzer at 1.4 T. Aqueous dispersions of citrate-coated MnPBA NPs at different concentrations were prepared and transferred into NMR tubes. Both the T_1 and T_2 relaxation times of these solutions were measured at 37 °C. The r_1 and r_2 relaxivity values were extracted from the linear plot of $(1/T_1)_{obs}$ and $(1/T_2)_{obs}$ versus Mn^{2+} concentration, respectively.

In Vivo Animal MRI Studies: All animal experiments were approved by the Kent State University's IACUC committee. Six-week-old mice (C57Bl6) were imaged with a Bruker ICON 1T solid-state MRI (Bruker, MA) to detect contrast enhancement before and after MnPBAs in vivo (Figure 2). The mice were preanesthetized with atropine/butorphanol and subsequently anesthetized with inhaled 5% isoflurane (2-chloro-2-(difluoromethoxy)-1,1,1-trifluoro-ethane) in oxygen, monitored throughout the imaging procedures, and maintained under isoflurane anesthesia (2%) and physiological temperatures. Scout images were taken to ensure proper orientation of the mouse, and T_1-weighted fast low angle shot (FLASH) scans were performed at time 0 (acquisition parameters for T_1: TE: 10 ms, TR: 4337.200 ms, Avg: 8, repetitions: 1 with a matrix size of $128 \times 128 \times 32$ and a field of view of 50 mm × 50 mm × 24 mm). Animals were next gavaged with MnPBAs (0.7×10^{-3} M in corn oil with a total volume of 0.25 mL) and imaged using the same protocol as above every 15 min for 2 h and 30 min. Anesthesia was terminated and the animal was allowed to recover in a warm cage. Images spanning the region of interest were *z*-compressed

using a maximum intensity projection and a look-up table applied to recolor the black and white pixels. Data processing was performed using ImageJ.

Statistical Analysis: Statistical analysis was performed using GraphPad Prism version 8.0 software. The in vitro studies were run with at least three biological replicates, and each biological replicate had three technical replicates. A two-tailed unpaired *t*-test was used to determine statistical significance between two groups. A statistical significance among multiple groups was analyzed using one-way analysis of variant (ANOVA) followed by the Holm–Sidak comparisons test. For all analyses, a *p*-value of less than 0.05 was considered to be statistically significant. Data were presented as mean ± standard deviation (mean ± s.d.).

Supporting Information

Supporting Information is available from the Wiley Online Library or from the author.

Acknowledgements

The TEM data reported in this work were obtained using the Cryo TEM Facility at Liquid Crystal Institute, KSU that is supported by the Ohio Research Scholars Program.

Conflict of Interest

The authors declare no conflict of interest.

Data Availability Statement

The data that support the findings of this study are available from the corresponding author upon reasonable request.

Keywords

biocompatible coordination polymers, contrast agents, magnetic resonance imaging, manganese compounds with water coordination, nanoparticles, Prussian blue, relaxivity

Received: May 20, 2021
Revised: July 19, 2021
Published online: August 11, 2021

[1] K. R. Dunbar, R. A. Heintz, *Prog. Inorg. Chem.* **1997**, *45*, 283.
[2] M. Ware, *J. Chem. Educ.* **2008**, *85*, 612.
[3] Research, U. S. F. a. D. A. C. f. D. E. a. *Questions and Answers on Prussian Blue*, http://www.fda.gov/cder/drug/infopage/prussian_blue/Q&A.htm (accessed: September 2016).
[4] M. Shokouhimehr, E. S. Soehnlen, A. Khitrin, S. Basu, S. D. Huang, *Inorg. Chem. Commun.* **2010**, *13*, 58.
[5] M. Shokouhimehr, E. S. Soehnlen, J. Hao, M. Griswold, C. Flask, X. Fan, J. P. Basilion, S. Basu, S. D. Huang, *J. Mater. Chem.* **2010**, *20*, 5251.
[6] E. Chelebaeva, J. Larionova, Y. Guari, R. A. Ferreira, L. D. Carlos, A. A. Trifonov, T. Kalaivani, A. Lascialfari, C. Guérin, K. Molvinger, *Nanoscale* **2011**, *3*, 1200.
[7] H. Xia, Y. Wan, G. Yuan, Y. Fu, X. Wang, *J. Power Sources* **2013**, *241*, 486.
[8] H. Y. Lian, M. Hu, C. H. Liu, Y. Yamauchi, K. C. W. Wu, *Chem. Commun.* **2012**, *48*, 5151.
[9] M. Perrier, S. Kenouche, J. R. M. Long, K. Thangavel, J. Larionova, C. Goze-Bac, A. Lascialfari, M. Mariani, N. Baril, C. Guerin, *Inorg. Chem.* **2013**, *52*, 13402.
[10] Q. Jin, C. l. Xie, Y. J. Wu, Y. l. Liu, *New Carbon Mater.* **2012**, *27*, 123.
[11] G. Paul, Y. Prado, N. Dia, E. Rivière, S. Laurent, M. Roch, L. Vander Elst, R. N. Muller, L. Sancey, P. Perriat, *Chem. Commun.* **2014**, *50*, 6740.
[12] M. F. Dumont, H. A. Hoffman, P. R. Yoon, L. S. Conklin, S. R. Saha, J. Paglione, R. W. Sze, R. Fernandes, *Bioconjugate Chem.* **2014**, *25*, 129.
[13] S. Mukherjee, B. R. Rao, B. Sreedhar, P. Paik, C. R. Patra, *Chem. Commun.* **2015**, *51*, 7325.
[14] J. Long, Y. Guari, C. Guérin, J. Larionova, *Dalton Trans.* **2016**, *45*, 17581.
[15] Z. Qin, Y. Li, N. Gu, *Adv. Healthcare Mater.* **2018**, *7*, 1800347.
[16] R. B. Lauffer, *Chem. Rev.* **1987**, *87*, 901.
[17] P. Caravan, J. J. Ellison, T. J. McMurry, R. B. Lauffer, *Chem. Rev.* **1999**, *99*, 2293.
[18] A. S. Merbach, L. Helm, E. Toth, *The Chemistry of Contrast Agents in Medical Magnetic Resonance Imaging*, John Wiley & Sons, Hoboken, NJ **2013**.
[19] S. Aime, M. Botta, E. Terreno, *Adv. Inorg. Chem.* **2005**, *57*, 173.
[20] S. Aime, M. Botta, M. Fasano, E. Terreno, *Chem. Soc. Rev.* **1998**, *27*, 19.
[21] H. B. Na, J. H. Lee, K. An, Y. I. Park, M. Park, I. S. Lee, D. H. Nam, S. T. Kim, S. H. Kim, S. W. Kim, *Angew. Chem.* **2007**, *119*, 5493.
[22] J. Kowalewski, K. M. Larsson, *Chem. Phys. Lett.* **1985**, *119*, 157.
[23] P. Caravan, *Chem. Soc. Rev.* **2006**, *35*, 512.
[24] S. Kaminsky, M. Laniado, M. Gogoll, W. Kornmesser, W. Clauss, M. Langer, C. Claussen, R. Felix, *Radiology* **1991**, *178*, 503.
[25] T. H. P. Rijcken, M. A. Davis, P. R. Ros, *J. Magn. Reson. Imaging* **1994**, *4*, 291.
[26] W. C. Small, D. DeSimone-Macchi, J. R. Parker, A. Sukerkar, P. F. Hahn, D. L. Rubin, J. V. Zelch, J. E. Kuhlman, E. K. Outwater, J. C. Weinreb, *J. Magn. Reson. Imaging* **1999**, *10*, 15.
[27] A. Giovagnoni, A. Fabbri, F. Maccioni, *Abdom. Imaging.* **2002**, *27*, 367.
[28] S. D. Huang, A. K. Khitrin, V. S. Perera, M. S. Kandanapitiye, Nanoparticulate manganese MRI contrast agents. *US Patent 9, 198, 988*, **2015**.
[29] J. S. Renny, L. L. Tomasevich, E. H. Tallmadge, D. B. Collum, *Angew. Chem., Int. Ed.* **2013**, *52*, 11998.
[30] K. Nakamoto, *Handbook of Vibrational Spectroscopy*, John Wiley & Sons, Hoboken, NJ **2006**.
[31] A. Bjørnerud, L. Johansson, *NMR Biomed.* **2004**, *17*, 465.
[32] S. Laurent, D. Forge, M. Port, A. Roch, C. Robic, L. Vander Elst, R. N. Muller, *Chem. Rev.* **2008**, *108*, 2064.
[33] W. Zhu, K. Liu, X. Sun, X. Wang, Y. Li, L. Cheng, Z. Liu, *ACS Appl. Mater. Interfaces* **2015**, *7*, 11575.
[34] Secondary Drinking Water Standards: Guidance for Nuisance Chemicals. https://www.epa.gov/sdwa/secondary-drinking-water-standards-guidance-nuisance-chemicals. Access in July, 2021.
[35] Agency, U. S. E. P. Drinking Water Contaminants–Standards and Regulations. https://19january2017snapshot.epa.gov/dwstandardsregulations_.htmL. Access in July, 2021.
[36] J. Vetter, *Toxicon* **2000**, *38*, 11.